

¹ A Gaussian process model of human electrocorticographic
² data

³ Lucy L. W. Owen¹, Andrew C. Heusser^{1,2}, and Jeremy R. Manning^{1*}

¹Department of Psychological and Brain Sciences, Dartmouth College,
Hanover, NH 03755, USA

²Akili Interactive,
Boston, MA 02110, USA

⁴ **Abstract**

We present a model-based method for inferring full-brain neural activity at millimeter-scale spatial resolutions and millisecond-scale temporal resolutions using standard human intracranial recordings. Our approach assumes that different people's brains exhibit similar correlational structure, and that activity and correlation patterns vary smoothly over space. One can then ask, for an arbitrary individual's brain: given recordings from a limited set of locations in that individual's brain, along with the observed spatial correlations learned from other people's recordings, how much can be inferred about ongoing activity at *other* locations throughout that individual's brain? We show that our approach generalizes across people and tasks, thereby providing a person- and task-general means of inferring high spatiotemporal resolution full-brain neural dynamics from standard low-density intracranial recordings.

Keywords: Electrocorticography (ECoG), intracranial electroencephalography (iEEG), local field potential (LFP), epilepsy, maximum likelihood estimation, Gaussian process regression

¹⁹ **Introduction**

²⁰ Modern human brain recording techniques are fraught with compromise [33]. Commonly used
²¹ approaches include functional magnetic resonance imaging (fMRI), scalp electroencephalogra-
²² phy (EEG), and magnetoencephalography (MEG). For each of these techniques, neuroscientists
²³ and electrophysiologists must choose to optimize spatial resolution at the cost of temporal reso-
²⁴ lution (e.g., as in fMRI) or temporal resolution at the cost of spatial resolution (e.g., as in EEG and
²⁵ MEG). A less widely used approach (due to requiring work with neurosurgical patients) is to
²⁶ record from electrodes implanted directly onto the cortical surface (electrocorticography; ECoG)

27 or into deep brain structures (intracranial EEG; iEEG). However, these intracranial approaches
28 also require compromise: the high spatiotemporal resolution of intracranial recordings comes
29 at the cost of substantially reduced brain coverage, since safety considerations limit the number
30 of electrodes one may implant in a given patient’s brain. Further, the locations of implanted
31 electrodes are determined by clinical, rather than research, needs.

32 An increasingly popular approach is to improve the effective spatial resolution of MEG or
33 scalp EEG data by using a geometric approach called *beamforming* to solve the biomagnetic or
34 bioelectrical inverse problem [28]. This approach entails using detailed brain conductance mod-
35 els (often informed by high spatial resolution anatomical MRI images) along with the known
36 sensor placements (localized precisely in 3D space) to reconstruct brain signals originating from
37 theoretical point sources deep in the brain (and far from the sensors). Traditional beamforming
38 approaches must overcome two obstacles. First, the inverse problem beamforming seeks to
39 solve has infinitely many solutions. Researchers have made traction towards constraining the
40 solution space by assuming that signal-generating sources are localized on a regularly spaced
41 grid spanning the brain and that individual sources are small relative to their distances to the
42 sensors [1, 11, 34]. The second, and in some ways much more serious, obstacle is that the
43 magnetic fields produced by external (noise) sources are substantially stronger than those pro-
44 duced by the neuronal changes being sought (i.e., at deep structures, as measured by sensors
45 at the scalp). This means that obtaining adequate signal quality often requires averaging the
46 measured responses over tens to hundreds of responses or trials (e.g., see review by [11]).

47 Another approach to obtaining high spatiotemporal resolution neural data has been to col-
48 lect fMRI and EEG data simultaneously. Simultaneous fMRI-EEG has the potential to balance
49 the high spatial resolution of fMRI with the high temporal resolution of scalp EEG, thereby,
50 in theory, providing the best of both worlds. In practice, however, the signal quality of both
51 recordings suffers substantially when the two techniques are applied simultaneously (e.g., see

52 review by [13]). In addition, the experimental designs that are ideally suited to each technique
53 individually are somewhat at odds. For example, fMRI experiments often lock stimulus presen-
54 tation events to the regularly spaced image acquisition time (TR), which maximizes the number
55 of post-stimulus samples. By contrast, EEG experiments typically employ jittered stimulus pre-
56 sentation times to maximize the experimentalist’s ability to distinguish electrical brain activity
57 from external noise sources such as from 60 Hz alternating current power sources.

58 The current “gold standard” for precisely localizing signals and sampling at high temporal
59 resolution is to take (ECoG or iEEG) recordings from implanted electrodes (but from a limited
60 set of locations in any given brain). This begs the following question: what can we infer about
61 the activity exhibited by the rest of a person’s brain, given what we learn from the limited
62 intracranial recordings we have from their brain and additional recordings taken from *other*
63 people’s brains? Here we develop an approach, which we call *SuperEEG*¹, based on Gaussian
64 process regression [27]. SuperEEG entails using data from multiple people to estimate activ-
65 ity patterns at arbitrary locations in each person’s brain (i.e., independent of their electrode
66 placements). We test our SuperEEG approach using two large datasets of intracranial record-
67 ings [7, 8, 12, 16–19, 21, 23, 30–32, 35, 41]. We show that the SuperEEG algorithm recovers
68 signals well from electrodes that were held out of the training dataset. We also examine the
69 factors that influence how accurately activity may be estimated (recovered), which may have
70 implications for electrode design and placement in neurosurgical applications.

71 Approach

72 The SuperEEG approach to inferring high temporal resolution full-brain activity patterns is
73 outlined and summarized in Figure 1. We describe (in this section) and evaluate (in *Results*) our

¹The term “SuperEEG” was coined by Robert J. Sawyer in his popular science fiction novel *The Terminal Experiment* [29]. SuperEEG is a fictional technology that measures ongoing neural activity throughout the entire living human brain with perfect precision and at arbitrarily high spatiotemporal resolution.

74 approach using a two large previously collected dataset comprising multi-session intracranial
75 recordings. Dataset 1 comprises multi-session recordings taken from 6876 electrodes implanted
76 in the brains of 88 epilepsy patients [21, 23, 30–32]. Each recording session lasted from 0.2–
77 3 h (total recording time: 0.3–14.2 h; Fig. S4E). During each recording session, the patients
78 participated in a free recall list learning task, which lasted for up to approximately 1 h. In
79 addition, the recordings included “buffer” time (the length varied by patient) before and after
80 each experimental session, during which the patients went about their regular hospital activities
81 (confined to their hospital room, and primarily in bed). These additional activities included
82 interactions with medical staff and family, watching television, reading, and other similar
83 activities. For the purposes of the Dataset 1 analyses presented here, we aggregated all data
84 across each recording session, including recordings taken during the main experimental task
85 as well as during non-experimental time. We used Dataset 1 to develop our main SuperEEG
86 approach, and to examine the extent to which SuperEEG might be able to generate task-general
87 predictions. Dataset 2 comprised multi-session recordings from 4436 electrodes implanted in
88 the brains of 40 epilepsy patients [7, 8, 12, 16–19, 35, 41]. Each recording session lasted from
89 0.4–2.2 h (total recording time: 0.4–6.6 h; Fig. S4K). Whereas Dataset 1 included recordings
90 taken as the patients participated in a variety of activities, Dataset 2 included recordings taken
91 as each patient performed each of two specific experimental memory tasks: a random word list
92 free recall task (Experiment 1) and a categorized word list free recall task (Experiment 2). We
93 used Dataset 2 to further examine the ability of SuperEEG to generalize its predictions within
94 versus across tasks. Figure S4 provides additional information about both datasets.

95 We first applied fourth order Butterworth notch filter to remove 60 Hz ($\pm .5$ Hz) line noise
96 from every recording (from every electrode). Next, we downsampled the recordings (regardless
97 of the original samplerate) to 250 Hz. (This downsampling step served to both normalize for
98 differences in sampling rates across patients and to ease the computational burden of our sub-

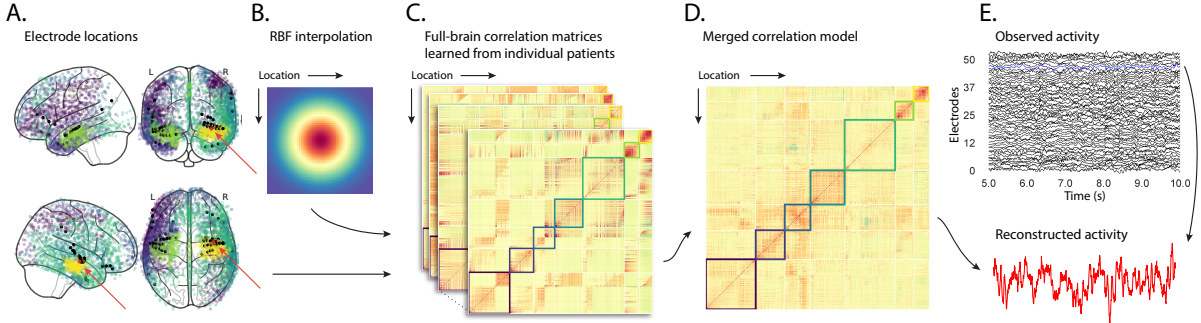


Figure 1: Methods overview. **A. Electrode locations.** Each dot reflects the location of a single electrode implanted in the brain of a Dataset 1 patient. A held-out recording location from one patient is indicated in red, and the patient’s remaining electrodes are indicated in black. The electrodes from the remaining patients are colored by k -means cluster (computed using the full-brain correlation model shown in Panel D). **B. Radial basis function kernel.** Each electrode contributed by the patient (black) weights on the full set of locations under consideration (all dots in Panel A, defined as \bar{R} in the text). The weights fall off with positional distance (in MNI space) according to an RBF. **C. Per-patient correlation matrices.** After computing the pairwise correlations between the recordings from each patient’s electrodes, we use RBF-weighted averages to estimate correlations between all locations in \bar{R} . We obtain an estimated full-brain correlation matrix using each patient’s data. **D. Merged correlation model.** We combine the per-patient correlation matrices (Panel C) to obtain a single full-brain correlation model that captures information contributed by every patient. Here we have sorted the rows and columns to reflect k -means clustering labels [using $k=7$; 42], whereby we grouped locations based on their correlations with the rest of the brain (i.e., rows of the matrix displayed in the panel). The boundaries denote the cluster groups. The rows and columns of Panel C have been sorted using the Panel D-derived cluster labels. **E. Reconstructing activity throughout the brain.** Given the observed recordings from the given patient (shown in black; held-out recording is shown in blue), along with a full-brain correlation model (Panel D), we use Equation 12 to reconstruct the most probable activity at the held-out location (red).

99 sequent analyses.) We then excluded any electrodes that showed putative epileptiform activity.
100 Specifically, we excluded from further analysis any electrode that exhibited an average kurtosis
101 of 10 or greater across all of that patient’s recording sessions. We also excluded any patients
102 with fewer than 2 electrodes that passed this criteria, as the SuperEEG algorithm requires
103 measuring correlations between 2 or more electrodes from each patient. For Dataset 1, this
104 yielded clean recordings from 4168 electrodes implanted throughout the brains of 67 patients
105 (Fig. 1A); for Dataset 2, this yielded clean recordings from 3159 electrodes from 24 patients.
106 Each individual patient contributes electrodes from a limited set of brain locations, which we
107 localized in a common space [MNI152; 10]; an example Dataset 1 patient’s 54 electrodes that
108 passed the above kurtosis threshold test are highlighted in black and red.

The recording from a given electrode is maximally informative about the activity of the neural tissue immediately surrounding its recording surface. However, brain regions that are distant from the recording surface of the electrode also contribute to the recording, albeit (*ceteris paribus*) to a much lesser extent. One mechanism underlying these contributions is volume conduction. The precise rate of falloff due to volume conduction (i.e., how much a small volume of brain tissue at location x contributes to the recording from an electrode at location η) depends on the size of the recording surface, the electrode’s impedance, and the conductance profile of the volume of brain between x and η . As an approximation of this intuition, we place a Gaussian radial basis function (RBF) at the location η of each electrode’s recording surface (Fig. 1B). We use the values of the RBF at any brain location x as a rough estimate of how much structures around x contributed to the recording from location η :

$$\text{rbf}(x|\eta, \lambda) = \exp \left\{ -\frac{\|x - \eta\|^2}{\lambda} \right\}, \quad (1)$$

109 where the width variable λ is a parameter of the algorithm (which may in principle be set
110 according to location-specific tissue conductance profiles) that governs the level of spatial
111 smoothing. In choosing λ for the analyses presented here, we sought to maximize spatial

resolution (which implies a small value of λ) while also maximizing the algorithm's ability to generalize to any location throughout the brain, including those without dense electrode coverage (which implies a large value of λ). Here we set $\lambda = 20$, guided in part by our prior work [22, 24], and in part by examining the brain coverage with non-zero weights achieved by placing RBFs at each electrode location in Dataset 1 and taking the sum (across all electrodes) at each voxel in a 4 mm^3 MNI brain. (We then held λ fixed for our analyses of Dataset 2.) We note that this value could in theory be further optimized, e.g., using cross validation or a formal model [e.g., 24].

A second mechanism whereby a given region x can contribute to the recording at η is through (direct or indirect) anatomical connections between structures near x and η . We use temporal correlations in the data to estimate these anatomical connections [2]. Let \bar{R} be the set of locations at which we wish to estimate local field potentials, and let $R_s \subseteq \bar{R}$ be set of locations at which we observe local field potentials from patient s (excluding the electrodes that did not pass the kurtosis test described above). In the analyses below we define $\bar{R} = \cup_{s=1}^S R_s$. We can calculate the expected inter-electrode correlation matrix for patient s , where $C_{s,k}(i, j)$ is the correlation between the time series of voltages for electrodes i and j from subject s during session k , using:

$$\bar{C}_s = r\left(\frac{1}{n}\left(\sum_{k=1}^n z(C_{s,k})\right)\right), \text{ where} \quad (2)$$

$$z(r) = \frac{\log(1+r) - \log(1-r)}{2} \text{ is the Fisher } z\text{-transformation and} \quad (3)$$

$$z^{-1}(z) = r(z) = \frac{\exp(2z) - 1}{\exp(2z) + 1} \text{ is its inverse.} \quad (4)$$

Next, we use Equation 1 to construct a number of to-be-estimated locations by number of patient electrode locations weight matrix, W_s . Specifically, W_s approximates how informative the recordings at each location in R_s are in reconstructing activity at each location in \bar{R} , where

¹³² the contributions fall off with an RBF according to the distances between the corresponding
¹³³ locations:

$$W_s(i, j) = \text{rbf}(i|j, \lambda). \quad (5)$$

¹³⁴ Given this weight matrix, W_s , and the observed inter-electrode correlation matrix for patient
¹³⁵ s , \bar{C}_s , we can estimate the correlation matrix for all locations in \bar{R} (\hat{C}_s ; Fig. 1C) using:

$$\hat{N}_s(x, y) = \sum_{i=1}^{|R_s|} \sum_{j=1}^{i-1} W(x, i) \cdot W(y, j) \cdot z(\bar{C}_s(i, j)) \quad (6)$$

$$\hat{D}_s(x, y) = \sum_{i=1}^{|R_s|} \sum_{j=1}^{i-1} W(x, i) \cdot W(y, j). \quad (7)$$

$$\hat{C}_s = r\left(\frac{\hat{N}_s}{\hat{D}_s}\right). \quad (8)$$

After estimating the numerator (\hat{N}_s) and denominator (\hat{D}_s) placeholders for each \hat{C}_s , we aggregate these estimates across the S patients to obtain a single expected full-brain correlation matrix (\hat{K} ; Fig. 1D):

$$\hat{K} = r\left(\frac{\sum_{s=1}^S \hat{N}_s}{\sum_{s=1}^S \hat{D}_s}\right). \quad (9)$$

¹³⁶ Intuitively, the numerators capture the general structures of the patient-specific estimates of full-
¹³⁷ brain correlations, and the denominators account for which locations were near the implanted
¹³⁸ electrodes in each patient. To obtain \hat{K} , we compute a weighted average across the estimated
¹³⁹ patient-specific full-brain correlation matrices, where patients with observed electrodes near a
¹⁴⁰ particular set of locations in \hat{K} contribute more to the estimate.

¹⁴¹ Having used the multi-patient data to estimate a full-brain correlation matrix at the set
¹⁴² of locations in \bar{R} that we wish to know about, we next use \hat{K} to estimate activity patterns
¹⁴³ everywhere in \bar{R} , given observations at only a subset of locations in \bar{R} (Fig. 1E).

144 Let α_s be the set of indices of patient s 's electrode locations in \bar{R} (i.e., the locations in R_s),
 145 and let β_s be the set of indices of all other locations in \bar{R} . In other words, β_s reflects the locations
 146 in \bar{R} where we did not observe a recording for patient s (these are the recording locations we
 147 will want to fill in using SuperEEG). We can sub-divide \hat{K} as follows:

$$\hat{K}_{\beta_s, \alpha_s} = \hat{K}(\beta_s, \alpha_s), \text{ and} \quad (10)$$

$$\hat{K}_{\alpha_s, \alpha_s} = \hat{K}(\alpha_s, \alpha_s). \quad (11)$$

148 Here $\hat{K}_{\beta_s, \alpha_s}$ represents the correlations between the “unknown” activity at the locations indexed
 149 by β_s and the observed activity at the locations indexed by α_s , and $\hat{K}_{\alpha_s, \alpha_s}$ represents the
 150 correlations between the observed recordings (at the locations indexed by α_s).

151 Let Y_{s,k,α_s} be the number-of-timepoints (T) by $|\alpha_s|$ matrix of (observed) voltages from the
 152 electrodes in α_s during session k from patient s . Then we can estimate the voltage from patient
 153 s 's k^{th} session at the locations in β_s using [27]:

$$\hat{Y}_{s,k,\beta_s} = ((\hat{K}_{\beta_s, \alpha_s} \cdot \hat{K}_{\alpha_s, \alpha_s}^{-1}) \cdot Y_{s,k,\alpha_s}^T)^T. \quad (12)$$

154 This equation is the foundation of the SuperEEG algorithm. Whereas we observe recordings
 155 only at the locations indexed by α_s , Equation 12 allows us to estimate the recordings at all loca-
 156 tions indexed by β_s , which we can define *a priori* to include any locations we wish, throughout
 157 the brain. This yields estimates of the time-varying voltages at *every* location in \bar{R} , provided that
 158 we define \bar{R} in advance to include the union of all of the locations in R_s and all of the locations
 159 at which we wish to estimate recordings (i.e., a timeseries of voltages).

160 We designed our approach to be agnostic to electrode impedances, as electrodes that do not
 161 exist do not have impedances. Therefore our algorithm recovers voltages in standard deviation
 162 (z -scored) units rather than attempting to recover absolute voltages. (This property reflects the

fact that $\hat{K}_{\beta_s, \alpha_s}$ and $\hat{K}_{\alpha_s, \alpha_s}$ are correlation matrices rather than covariance matrices.) Also, we note that Equation 12 requires computing a T by T matrix, which can become computationally intractable when T is very large (e.g., for the patient highlighted in Fig. 2, $T = 12786750$). However, because Equation 12 is time invariant, we may compute Y_{s,k,β_s} in a piecewise manner by filling in Y_{s,k,β_s} one row at a time (using the corresponding samples from Y_{s,k,α_s}).

The SuperEEG algorithm described above and in Figure 1 allows us to estimate, up to a constant scaling factor, local field potentials (LFPs) for each patient at all arbitrarily chosen locations in the set \bar{R} , even if we did not record that patient's brain at all of those locations. We next turn to an evaluation of the accuracy of those estimates.

Results

We used a cross-validation approach to test the accuracy with which the SuperEEG algorithm reconstructs activity throughout the brain. For each patient in turn, we estimated full-brain correlation matrices (Eqn. 9) using data from all of the *other* patients. This step ensured that the data we were reconstructing could not also be used to estimate the between-location correlations that drove the reconstructions via Equation 12 (otherwise the analysis would be circular). For that held-out patient, we held out each electrode in turn. We used Equation 12 to reconstruct activity at the held-out electrode location, using the correlation matrix learned from all other patients' data as \hat{K} , and using activity recorded from the other electrodes from the held-out patient as Y_{s,k,α_s} . We then asked: how closely did each of the SuperEEG-estimated recordings at those electrodes match the observed recordings from those electrodes (i.e., how closely did the estimated \hat{Y}_{s,k,β_s} match the observed Y_{s,k,β_s})?

To illustrate our approach, we first examine an individual held-out raw LFP trace and its associated SuperEEG-derived reconstruction. Figure 2A displays the observed LFP from the red electrode in Figure 1A (blue), and its associated reconstruction (red), during the 5 s time

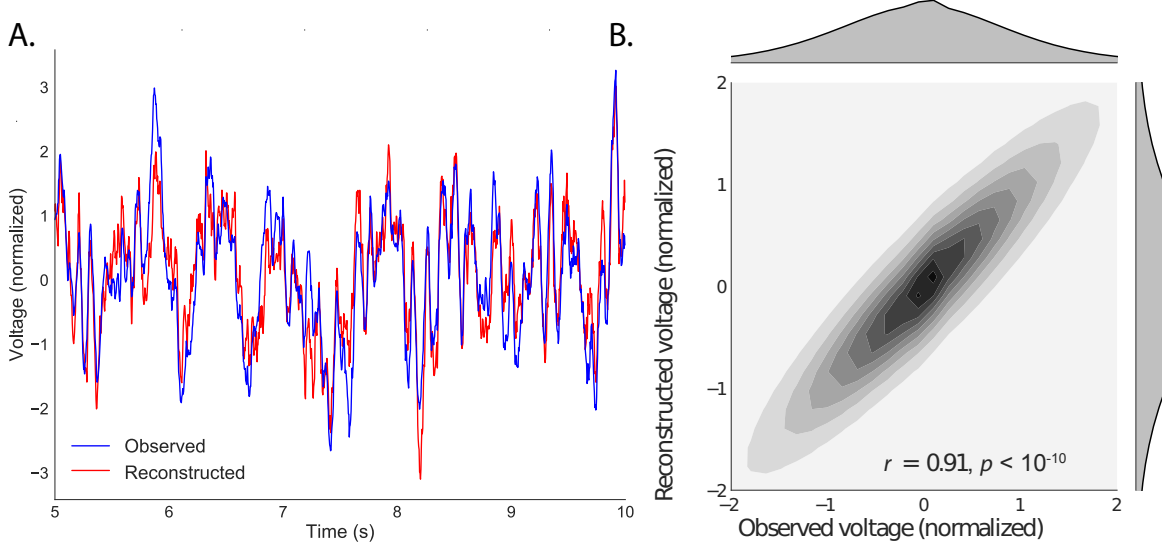


Figure 2: Observed and reconstructed LFP from a single electrode. **A. Example LFP.** A 5 s recording from the red electrode in Figure 1A is displayed in blue, and the reconstructed LFP during the same time window is shown in red. **B. Observed versus reconstructed LFP over 14.2 hours.** The two-dimensional histogram reflects the relation between distributions of observed versus reconstructed voltages from one patient, across the 14.2 hours of recorded data collected over 6 recording sessions. The correlation reported in the panel is between the observed and reconstructed voltages. Both panels: all voltages are represented in standard deviation units (computed within session).

187 window during one of the example patient's six recording sessions shown in Figure 1E. The
 188 two traces match closely ($r = 0.86, p < 10^{-10}$). Figure 2B displays a two-dimensional histogram
 189 of the actual versus reconstructed voltages for the entire 14.2 total hours of recordings from the
 190 example electrode (correlation: $r = 0.91, p < 10^{-10}$). This example confirms that the SuperEEG
 191 algorithm recovers the recordings from this single electrode well. Next, we used this general
 192 approach to quantify the algorithm's performance across the full dataset.

193 For each held-out electrode, from each held-out patient in turn, we computed the average
 194 correlation (across recording sessions) between the SuperEEG-reconstructed voltage traces and
 195 the observed voltage traces from that electrode. For this analysis we set \bar{R} to be the union of
 196 all electrode locations across all patients. This yielded a single correlation coefficient for each

197 electrode location in \bar{R} , reflecting how well the SuperEEG algorithm was able to recover the
198 recording at that location by incorporating data across patients (black histogram in Fig. 3A, map
199 in Fig. 3C). The observed distribution of correlations was centered well above zero (mean: 0.52;
200 t -test comparing mean of distribution of z -transformed average patient correlation coefficients
201 to 0: $t(66) = 25.08, p < 10^{-10}$), indicating that the SuperEEG algorithm recovers held-out activity
202 patterns substantially better than random guessing.

203 As a stricter benchmark, we compared the quality of these across-participant reconstructions
204 (i.e., computed using a correlation model learned from other patients' data) to reconstructions
205 generated using a correlation model trained using the in-patient's data. In other words, for
206 this within-patient benchmark analysis we estimated \hat{C}_s (Eqn. 8) for each patient in turn, using
207 recordings from all of that patient's electrodes except at the location we were reconstructing.
208 These within-patient reconstructions serve as an estimate of how well data from all of the
209 other electrodes from that single patient may be used to estimate held-out data from the
210 same patient. This allows us to ask how much information about the activity at a given
211 electrode might be inferred through (a) volume conductance or other sources of "leakage"
212 from activity patterns measured from the patient's other electrodes and (b) across-electrode
213 correlations learned from that single patient. As shown in Figure 3A (gray histogram), the
214 distribution of within-patient correlations was centered well above zero (mean: 0.32; t -test
215 comparing mean of distribution of z -transformed average patient correlation coefficients to 0:
216 $t(66) = 15.16, p < 10^{-10}$). However, the across-patient correlations were substantially higher
217 (t -test comparing average z -transformed within versus across patient electrode correlations:
218 $t(66) = 9.62, p < 10^{-10}$). This is an especially conservative test, given that the across-patient
219 SuperEEG reconstructions exclude (from the correlation matrix estimates) all data from the
220 patient whose data is being reconstructed. We repeated each of these analyses on a second
221 independent dataset and found similar results (Fig. 3B, D; within versus across reconstruction

accuracy: $t(23) = 6.93, p < 10^{-5}$). We also replicated this result separately for each of the two experiments from Dataset 2 (Fig. S1). This overall finding, that reconstructions of held-out data using correlation models learned from *other* patient's data yield higher reconstruction accuracy than correlation models learned from the patient whose data is being reconstructed, has two important implications. First, it implies that distant electrodes provide additional predictive power to the data reconstructions beyond the information contained solely in nearby electrodes. (This follows from the fact that each patient's grid, strip, and depth electrodes are implanted in a unique set of locations, so for any given electrode the closest electrodes in the full dataset tend to come from the same patient.) Second, it implies that the spatial correlations learned using the SuperEEG algorithm are, to some extent, similar across people.

The recordings we analyzed from Dataset 1 comprised data collected as the patients performed a variety of (largely idiosyncratic) tasks throughout each day's recording session. That we observed reliable reconstruction accuracy across patients suggests that the spatial correlations derived from the SuperEEG algorithm are, to some extent, similar across tasks. We tested this finding more directly using Dataset 2. In Dataset 2, the recordings were limited to times when each patient was participating in each of two experiments (Experiment 1, a random-word list free recall task, and Experiment 2, a categorized list free recall task). We wondered whether a correlation model learned from data from one experiment might yield good predictions of data from the other experiment. Further, we wondered about the extent to which it might be beneficial or harmful to combine data across tasks.

To test the task-specificity of the SuperEEG-derived correlation models, we repeated the above within- and across-patient cross validation procedures separately for Experiment 1 and Experiment 2 data from Dataset 2. We then compared the reconstruction accuracies for held-out electrodes, for models trained within versus across the two experiments, or combining across both experiments (Fig. S2). In every case we found that across-patient models trained using

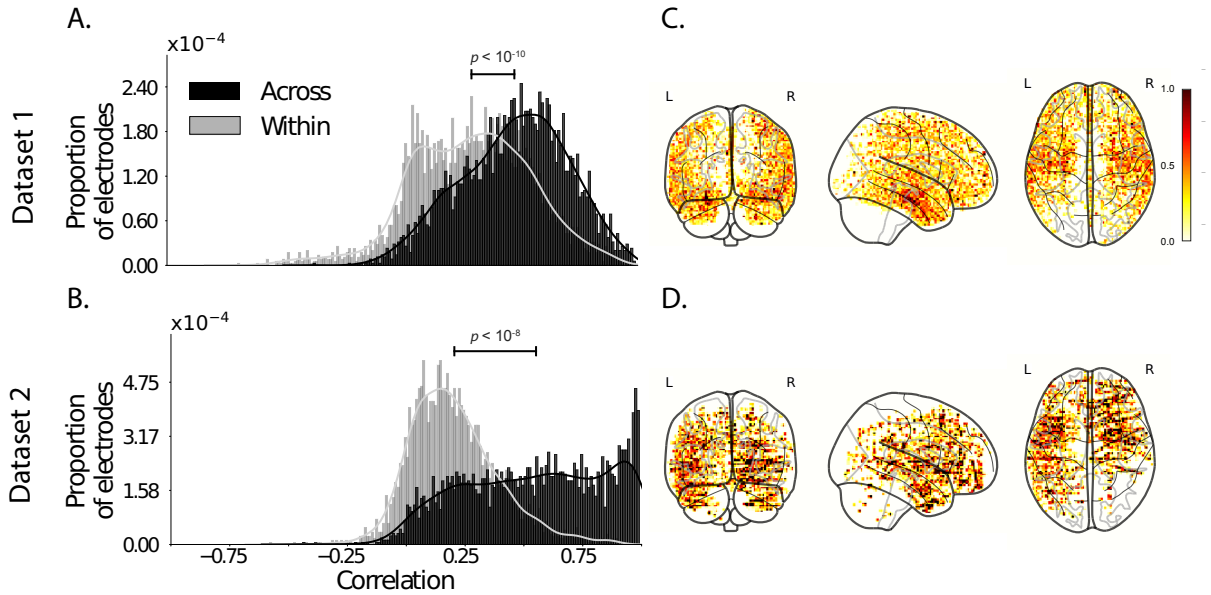


Figure 3: Reconstruction quality across all electrodes in two ECoG datasets. A. Distributions of correlations between observed versus reconstructed activity by electrode, for Dataset 1. The across-patient distribution (black) reflects reconstruction accuracy (correlation) using a correlation model learned from all but one patient’s data, and then applied to that held-out patient’s data. The within-patient distribution (gray) reflects performance using a correlation model learned from the same patient who contributed the to-be-reconstructed electrode. **B. Distributions of correlations for Dataset 2.** This panel is in the same format as Panel A, but reflects results obtained from Dataset 2. The histograms aggregate data across both Dataset 2 experiments; for results broken down by experiment see Figure S3. **C.–D. Reconstruction performance by location.** Each dot reflects the location of a single implanted electrode from Dataset 1 (Panel C) or Dataset 2 (Panel D). The dot colors denote the average across-session correlation, using the across-patient correlation model, between the observed and reconstructed activity at the given electrode location.

247 data from all other patients out-performed within-patient models trained on data only from the
248 subject contributing the given electrode ($ts(23) > 6.50, ps < 10^{-5}$). All reconstruction accuracies
249 also reliably exceeded chance performance ($ts(23) > 8.00, ps < 10^{-8}$). Average reconstruction
250 accuracy was highest for the across-patient models limited to data from the same experiment
251 (mean accuracy: 0.68); next-highest for the models that combined data across both experiments
252 (mean accuracy: 0.61); and lowest for models trained across tasks (mean accuracy: 0.47). This
253 result also held for each of the Dataset 2 experiments individually (Fig. S3). Taken together,
254 these results indicate that there are reliable commonalities in the spatial correlations of full-brain
255 activity across tasks, but that there are also reliable differences in these spatial correlations across
256 tasks. Whereas reconstruction accuracy benefits from incorporating data from other patients,
257 reconstruction accuracy is highest when constrained to within-task data, or data that includes
258 a variety of tasks (e.g., Dataset 1, or combining across the two Dataset 2 experiments).

259 Although both datasets we examined provide good full-brain coverage (when considering
260 data from every patient; e.g. Fig. 3C, D), electrodes are not placed uniformly throughout the
261 brain. For example, electrodes are more likely to be implanted in regions like the medial
262 temporal lobe (MTL), and are rarely implanted in occipital cortex (Fig. 4A, B). Separately for
263 each dataset, for each voxel in the 4 mm^3 voxel MNI152 brain, we computed the proportion
264 of electrodes in the dataset that were contained within a 20 MNI unit radius sphere centered
265 on that voxel. We defined the *density* at that location as this proportion. Across Datasets
266 1 and 2, the electrode placement densities were similar (correlation by voxel: $r = 0.56, p <$
267 10^{-10}). We wondered whether regions with good coverage might be associated with better
268 reconstruction accuracy (e.g. Fig. 3C, D indicate that many electrodes in the MTL have relatively
269 high reconstruction accuracy, and occipital electrodes tend to have relatively low reconstruction
270 accuracy). To test whether this held more generally across the entire brain, for each dataset
271 we computed the electrode placement density for each electrode from each patient (using

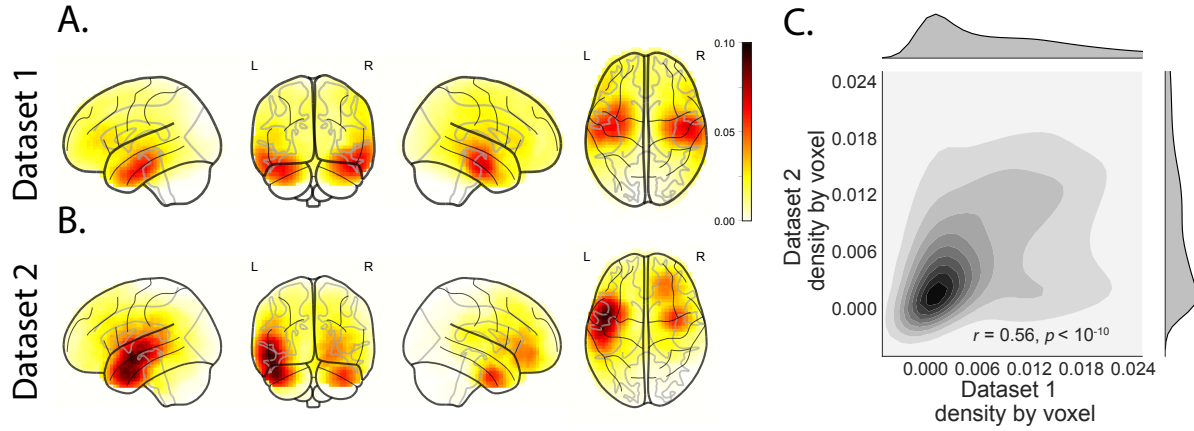


Figure 4: Electrode sampling density by location. **A. Electrode sampling density by voxel in Dataset 1.** Each voxel is colored by the proportion of total electrodes in the dataset that are located within a 20 MNI unit radius sphere centered on the given voxel. **B. Electrode sampling density by voxel in Dataset 2.** This panel displays the sampling density map for Dataset 2, in the same format as Panel A. **C. Correspondence in sampling density by voxel across Datasets 1 and 2.** The two-dimensional histogram displays the by-voxel densities in the two Datasets, and the one-dimensional histograms display the proportions of voxels in each dataset with the given density value. The correlation reported in the panel is across voxels in the 4 mm^3 MNI brain.

the proportion of *other* patients' electrodes within 20 MNI units of the given electrode). We then correlated these density values with the across-patient reconstruction accuracies for each electrode. Contrary to our expectation, rather than positive correlations, we found weak (but reliable) negative correlations between reconstruction accuracy and density for both datasets (Dataset 1: $r = -0.07, p < 10^{-5}$; Dataset 2: $r = -0.18, p < 10^{-10}$). This indicates that the reconstruction accuracies we observed are not driven solely by sampling density, but rather may also reflect higher order properties of neural dynamics such as functional correlations between distant voxels [3].

In neurosurgical applications where one wishes to infer full-brain activity patterns, can our framework yield insights into where the electrodes should be placed? A basic assumption of our approach (and of most prior ECoG work) is that electrode recordings are most informative about the neural activity near the recording surface of the electrode. But if we consider that activity

284 patterns throughout the brain are meaningfully correlated, are there particular implantation
285 locations that, if present in a patient’s brain, yield especially high reconstruction accuracies
286 throughout the rest of the brain? For example, one might hypothesize that brain structures
287 that are heavily interconnected with many other structures could be more informative about
288 full-brain activity patterns than comparatively isolated structures.

289 To gain insights into whether particular electrode locations might be especially informative,
290 we first computed the average reconstruction accuracy across all of each patient’s electrodes
291 (using the across-patients cross validation test; black histograms in Fig. 3A and B). We labeled
292 each patient’s electrodes in each dataset with the average reconstruction accuracy for that
293 patient. In other words, we assigned every electrode from each given patient the same value,
294 reflecting how well the activity patterns at those electrodes were reconstructed on average.
295 Next, for each voxel in the 4 mm³ MNI brain, we computed the average value across any
296 electrode (from any patient) that came within 20 MNI units of that voxel’s center. Effectively,
297 we computed an *information score* for each voxel, reflecting the average reconstruction accuracy
298 across any patients with electrodes near each voxel—where the averages were weighted to reflect
299 patients who had more electrodes implanted near that location. This yielded a single map for
300 each dataset, highlighting regions that are potentially promising implantation targets in terms
301 of providing full-brain activity information via SuperEEG (Fig. 5A, B). Despite task and patient
302 differences across the two datasets, we nonetheless found that the maps of the most promising
303 implantation targets derived from both datasets were similar (voxelwise correlation between
304 information scores across the two datasets: $r = 0.20, p < 10^{-10}$). While the correspondence
305 between the two maps was imperfect, our finding that there were some commonalities between
306 the two maps lends support to the notion that different brain areas are differently informative
307 about full-brain activity patterns. We also examined the intersection between the top 10% most
308 informative voxels across the two datasets (white outlines in Fig. 5A, B, Fig. S5). Supporting the

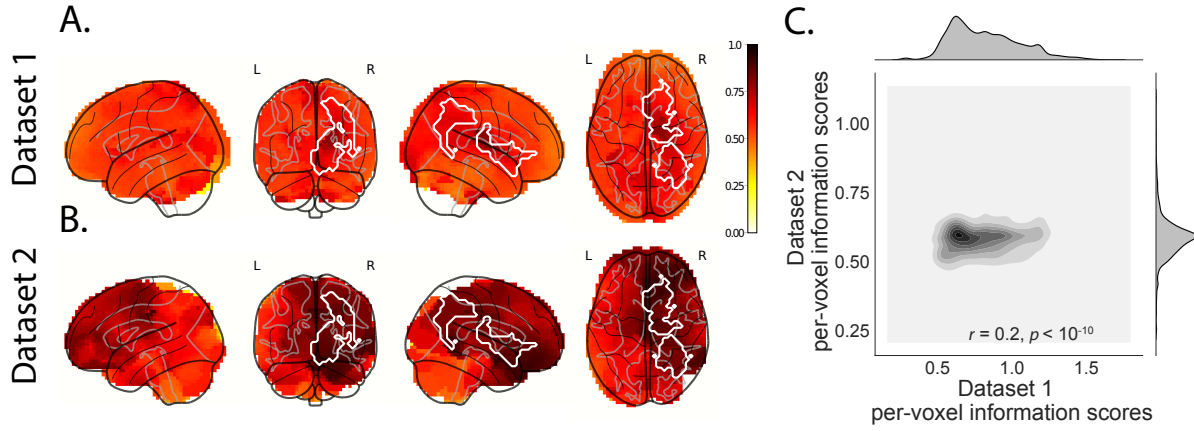


Figure 5: Most informative electrode locations. **A. Dataset 1 information score by voxel.** The voxel colors reflect the weighted average reconstruction accuracy across all electrodes from any patients with at least one electrode within 20 MNI units of the given voxel. **B. Dataset 2 information score by voxel.** This panel is in the same format as Panel A. In both panels the contours indicate the intersections between the top 10% most informative voxels in each map. **C. Correspondence in information scores by voxel across Datasets 1 and 2.** Same format as Figure 4C.

notion that structures that are highly interconnected with the rest of the brain might be especially good targets for implantation, this intersecting set of voxels with the highest information scores included major portions of the dorsal attention network (e.g., inferior parietal lobule, precuneus, inferior temporal gyrus, thalamus, and striatum) as well as some portions of the default mode network (e.g., angular gyrus) that are highly interconnected with a large proportion of the brain's gray matter [e.g., 39].

315 Discussion

Are our brain's networks static or dynamic? And to what extent are the network properties of our brains stable across people and tasks? One body of work suggests that our brain's *functional* networks are dynamic [e.g., 24], person-specific [e.g., 9], and task-specific [e.g., 40]. In contrast, although the gross anatomical structure of our brains changes meaningfully over the course of years as our brains develop, on the timescales of typical neuroimaging ex-

321 experiments (i.e., hours to days) our anatomical networks are largely stable [e.g., 4]. Further,
322 many aspects of brain anatomy, including white matter structure, are largely preserved across
323 people [e.g., 15, 26, 37]. There are several possible means of reconciling this apparent inconsis-
324 tency between dynamic person- and task-specific functional networks versus stable anatomical
325 networks. For example, relatively small magnitude anatomical differences across people may
326 be reflected in reliable functional connectivity differences. Along these lines, one recent study
327 found that diffusion tensor imaging (DTI) structural data is similar across people, but may be
328 used to predict person-specific resting state functional connectivity data [2]. Similarly, other
329 work indicates that task-specific functional connectivity may be predicted by resting state func-
330 tional connectivity data [5, 38]. Another (potentially complementary) possibility is that our
331 functional networks are constrained by anatomy, but nevertheless exhibit (potentially rapid)
332 task-dependent changes [e.g., 36].

333 Here we have taken a model-based approach to studying whether high spatiotemporal
334 resolution activity patterns throughout the human brain may be explained by a static connec-
335 tive model that is shared across people and tasks. Specifically, we trained a model to take
336 in recordings from a subset of brain locations, and then predicted activity patterns during the
337 same interval, but at *other* locations that were held out from the model. Our model, based on
338 Gaussian process regression, was built on three general hypotheses about the nature of the
339 correlational structure of neural activity (each of which we tested). First, we hypothesized that
340 functional correlations are stable over time and across tasks. We found that, although aspects of
341 the patients' functional correlations were stable across tasks, we achieved better reconstruction
342 accuracy when we trained the model on within-task data [we acknowledge that our general
343 approach could potentially be extended to better model across-task changes, following 5, 38,
344 and others]. Second, we hypothesized that some of the correlational structure of people's brain
345 activity is similar across individuals. Consistent with this hypothesis, our model explained the

346 data best when we trained the correlation model using data from *other* patients– even when
347 compared to a correlation model trained on the same patient’s data. Third, we resolved am-
348 biguities in the data by hypothesizing that neural activity from nearby sources will tend to be
349 similar, all else being equal. This hypothesis was supported through our finding that all of the
350 models we trained that incorporated this spatial smoothness assumption predicted held-out
351 data well above chance.

352 One potential limitation of our approach is that it does not provide a natural means of
353 estimating the precise timing of single-neuron action potentials. Prior work has shown that
354 gamma band and broadband activity in the LFP may be used to estimate the firing rates of
355 neurons that underly the population contributing to the LFP [6, 14, 20, 25]. Because SuperEEG
356 reconstructs LFPs throughout the brain, one could in principle use gamma or broadband power
357 in the reconstructed signals to estimate the corresponding firing rates (though not the timings
358 of individual action potentials).

359 Beyond providing a means of estimating ongoing activity throughout the brain using al-
360 ready implanted electrodes, our work also has implications for where to place the electrodes in
361 the first place. Electrodes are typically implanted to maximize coverage of suspected epilep-
362 togenic tissue. However, our findings suggest that this approach could be further optimized.
363 Specifically, one could leverage not only the non-invasive recordings taken during an initial
364 monitoring period (as is currently done routinely), but also recordings collected from other
365 patients. We could then ask: given what we learn from other patients’ data (and potentially
366 from the scalp EEG recordings of this new patient), where should we place a fixed number
367 of electrodes to maximize our ability to map seizure foci? As shown in Figures 5 and S5,
368 recordings from different locations are differently informative in terms of reconstructing the
369 spatiotemporal activity patterns throughout the brain. This property might be leveraged in
370 decisions about where to surgically implant electrodes in future patients.

³⁷¹ **Concluding remarks**

³⁷² Over the past several decades, neuroscientists have begun to leverage the strikingly profound
³⁷³ mathematical structure underlying the brain's complexity to infer how our brains carry out
³⁷⁴ computations to support our thoughts, actions, and physiological processes. Whereas tradition-
³⁷⁵ al beamforming techniques rely on geometric source-localization of signals measured at the
³⁷⁶ scalp, here we propose an alternative approach that leverages the rich correlational structure
³⁷⁷ of two large datasets of human intracranial recordings. In doing so, we are one step closer to
³⁷⁸ observing, and perhaps someday understanding, the full spatiotemporal structure of human
³⁷⁹ neural activity.

³⁸⁰ **Code availability**

³⁸¹ We have published an open-source toolbox implementing the SuperEEG algorithm. It may be
³⁸² downloaded [here](#). Additionally, we have provided code for all analyses and figures reported in
³⁸³ the current manuscript, available [here](#).

³⁸⁴ **Data availability**

³⁸⁵ The dataset analyzed in this study was generously shared by Michael J. Kahana. A portion of
³⁸⁶ Dataset 1 may be downloaded [here](#). Dataset 2 may be downloaded [here](#).

³⁸⁷ **Acknowledgements**

³⁸⁸ We are grateful for useful discussions with Luke J. Chang, Uri Hasson, Josh Jacobs, Michael J.
³⁸⁹ Kahana, and Matthijs van der Meer. We are also grateful to Michael J. Kahana for generously
³⁹⁰ sharing the ECoG data we analyzed in our paper, which was collected under NIMH grant
³⁹¹ MH55687 and DARPA RAM Cooperative Agreement N66001-14-2-4-032, both to M.J.K. Our
³⁹² work was also supported in part by NSF EPSCoR Award Number 1632738 and by a sub-award

393 of DARPA RAM Cooperative Agreement N66001-14-2-4-032 to J.R.M. The content is solely
394 the responsibility of the authors and does not necessarily represent the official views of our
395 supporting organizations.

396 Author Contributions

397 J.R.M conceived and initiated the project. L.L.W.O. and A.C.H. performed the analyses. J.R.M.
398 and L.L.W.O. wrote the manuscript.

399 Author Information

400 Reprints and permissions information is available at www.nature.com/reprints. The authors
401 declare no competing financial interests. Readers are welcome to comment on the online
402 version of the paper. Publisher's note: Springer Nature remains neutral with regard to jurisdic-
403 tional claims in published maps and institutional affiliations. Correspondence and requests for
404 materials should be addressed to J.R.M. (jeremy.r.manning@dartmouth.edu).

405 References

- 406 [1] Baillet, S., Mosher, J. C., and Leahy, R. M. (2001). Electromagnetic brain mapping. *IEEE*
407 *Signal Processing Magazine*, 18:14–30.
- 408 [2] Becker, C. O., Pequito, S., Pappas, G. J., Miller, M. B., adn D S Bassett, S. T. G., and Preciado,
409 V. M. (2018). Spectral mapping of brain functional connectivity from diffusion imaging.
410 *Scientific Reports*, 8(1411): <https://doi.org/10.1038/s41598-017-18769-x>.
- 411 [3] Betzel, R. F., Medaglia, J. D., Kahn, A. E., Soffer, J., Schonhaut, D. R., and Bassett, D. S.
412 (2017). Inter-regional ECoG correlations predicted by communication dynamics, geometry,
413 and correlated gene expression. *arXiv*, 1706.06088.

- 414 [4] Casey, B. J., Giedd, J. N., and Thomas, K. M. (2000). Structural and functional brain devel-
415 opment and its relation to cognitive development. *Biological Psychology*, 54(1–3):241–257.
- 416 [5] Cole, M. W., Ito, T., Bassett, D. S., and Schultz, D. H. (2016). Activity flow over resting-state
417 networks shapes cognitive task activations. *Nature Neuroscience*, 19(12):1718–1726.
- 418 [6] Crone, N. E., Korzeniewska, A., and Franaszczuk, P. (2011). Cortical gamma responses:
419 searching high and low. *International Journal of Psychophysiology*, 79(1):9–15.
- 420 [7] Ezzyat, Y., Kragel, J. E., Burke, J. F., Levy, D. F., Lyalenko, A., Wanda, P., O’Sullivan, L.,
421 Hurley, K. B., Busygin, S., Pedisich, I., Sperling, M. R., Worrell, G. A., Kucewicz, M. T., Davis,
422 K. A., Lucas, T. H., Inman, C. S., Lega, B. C., Jobst, B. C., Sheth, S. A., Zaghloul, K., Jutras,
423 M. J., Stein, J. M., Das, S. R., Gorniak, R., Rizzuto, D. S., and Kahana, M. J. (2017). Direct
424 brain stimulation modulates encoding states and memory performance in humans. *Current
425 Biology*, 27:1–8.
- 426 [8] Ezzyat, Y., Wanda, P. A., Levy, D. F., Kadel, A., Aka, A., Pedisich, I., Sperling, M. R.,
427 Sharan, A. D., Lega, B. C., Burks, A., Gross, R. E., Inman, C. S., Jobst, B. C., Goren-
428 stein, M. A., Davis, K. A., Worrell, G. A., Kucewicz, M. T., Stein, J. M., Gorniak, R.,
429 Das, S. R., Rizzuto, D. S., and Kahana, M. J. (2018). Closed-loop stimulation of tem-
430 poral cortex rescues functional networks and improves memory. *Nature Communications*,
431 9(365): <https://www.doi.org/10.1038/s41467-017-02753-0>.
- 432 [9] Finn, E. S., Shen, X., Scheinost, D., Rosenberg, M. D., Huang, J., Chun, M. M., Papademetris,
433 X., and Constable, R. T. (2015). Functional connectome fingerprinting: identifying individuals
434 using patterns of brain connectivity. *Nature Neuroscience*, 18:1664 – 1671.
- 435 [10] Grabner, G., Janke, A. L., Budge, M. M., Smith, D., Pruessner, J., and Collins, D. L. (2006).

- 436 Symmetric atlasing and model based segmentation: an application to the hippocampus in
437 older adults. *Medical Image Computing and Computer-Assisted Intervention*, 9:58–66.
- 438 [11] Hillebrand, A., Singh, K. D., Holliday, I. E., Furlong, P. L., and Barnes, G. R. (2005). A new
439 approach to neuroimaging with magnetoencephalography. *Human Brain Mapping*, 25:199–
440 211.
- 441 [12] Horak, P. C., Meisenhelter, S., Song, Y., Testorf, M. E., Kahana, M. J., Viles, W. D., Bujarski,
442 K. A., Connolly, A. C., Robbins, A. A., Sperling, M. R., Sharan, A. D., Worrell, G. A., Miller,
443 L. R., Gross, R. E., Davis, K. A., Roberts, D. W., Lega, B., Sheth, S. A., Zaghloul, K. A., Stein,
444 J. M., Das, S. R., Rizzuto, D. S., and Jobst, B. C. (2017). Interictal epileptiform discharges
445 impair word recall in multiple brain areas. *Epilepsia*, 58(3):373–380.
- 446 [13] Huster, R. J., Debener, S., Eichele, T., and Herrmann, C. S. (2012). Methods for simultaneous
447 EEG-fMRI: an introductory review. *The Journal of Neuroscience*, 32(18):6053–6060.
- 448 [14] Jacobs, J., Manning, J., and Kahana, M. (2010). Response to Miller: “Broadband” vs. “high
449 gamma” electrocorticographic signals. *Journal of Neuroscience*, 30(19).
- 450 [15] Jahanshad, N., Kochunov, P. V., Sprooten, E., Mandl, R. C., Nichols, T. E., Almasy, L.,
451 Blangero, J., Brouwer, R. M., Curran, J. E., de Zubiray, G. I., Duggirala, R., Fox, P. T., Hong,
452 L. E., Landman, B. A., Martin, N. G., McMahon, K. L., Medland, S. E., Mitchell, B. D., Olvera,
453 R. L., Peterson, C. P., Starr, J. M., Sussmann, J. E., Toga, A. W., Wardlaw, J. M., Wright, M. J.,
454 Pol, H. E. H., Pastin, M. E., McIntosh, A. M., Deary, I. J., Thompson, P. M., and Glahn, D. C.
455 (2013). Multi-site genetic analysis of diffusion images and voxelwise heritability analysis: A
456 pilot project of the enigma-dti working group. *NeuroImage*, 81(1):455–469.
- 457 [16] Kragel, J. E., Ezzyat, Y., Sperling, M. R., Gorniak, R., Worrell, G. A., Berry, B. M., Inman,
458 C., Lin, J.-J., Davis, K. A., Das, S. R., Stein, J. M., Jobst, B. C., Zaghloul, K. A., Sheth, S. A.,

- 459 Rizzuto, D. S., and Kahana, M. J. (2017). Similar patterns of neural activity predict memory
460 formation during encoding and retrieval. *NeuroImage*, 155:70–71.
- 461 [17] Kucewicz, M. T., Berry, B. M., Kremen, V., Brinkmann, B. H., Sperling, M. R., Jobst, B. C.,
462 Gross, R. E., Lega, B., Sheth, S. A., Stein, J. M., Das, S. R., Gorniak, R., Stead, S. M., Rizzuto,
463 D. S., Kahana, M. J., and Worrell, G. A. (2017). Dissecting gamma frequency activity during
464 human memory processing. *Brain*, 140:1337–1350.
- 465 [18] Kucewicz, M. T., Berry, B. M., Miller, L. R., Khadjevand, F., Ezzyat, Y., Stein, J. M., Kremen,
466 V., Brinkmann, B. H., Wanda, P., Sperling, M. R., Gorniak, R., Davis, K. A., Jobst, B. C., Gross,
467 R. E., Lega, B., Gompel, J. V., Stead, S. M., Rizzuto, D. S., Kahana, M. J., and Worrell, G. A.
468 (2018). Evidence for verbal memory enhancement with electrical brain stimulation in the
469 lateral temporal cortex. *Brain*, 141(4):971–978.
- 470 [19] Lin, J.-J., Rugg, M. D., Das, S., Stein, J., Rizzuto, D. S., Kahana, M. J., and Lega, B. C.
471 (2017). Theta band power increases in the posterior hippocampus predict successful episodic
472 memory encoding in humans. *Hippocampus*, 27:1040–1053.
- 473 [20] Manning, J. R., Jacobs, J., Fried, I., and Kahana, M. J. (2009). Broadband shifts in LFP power
474 spectra are correlated with single-neuron spiking in humans. *The Journal of Neuroscience*,
475 29(43):13613–13620.
- 476 [21] Manning, J. R., Polyn, S. M., Baltuch, G., Litt, B., and Kahana, M. J. (2011). Oscillatory
477 patterns in temporal lobe reveal context reinstatement during memory search. *Proceedings of
478 the National Academy of Sciences, USA*, 108(31):12893–12897.
- 479 [22] Manning, J. R., Ranganath, R., Norman, K. A., and Blei, D. M. (2014). Topographic
480 factor analysis: a Bayesian model for inferring brain networks from neural data. *PLoS One*,
481 9(5):e94914.

- 482 [23] Manning, J. R., Sperling, M. R., Sharan, A., Rosenberg, E. A., and Kahana, M. J. (2012).
483 Spontaneously reactivated patterns in frontal and temporal lobe predict semantic clustering
484 during memory search. *The Journal of Neuroscience*, 32(26):8871–8878.
- 485 [24] Manning, J. R., Zhu, X., Willke, T. L., Ranganath, R., Stachenfeld, K., Hasson, U., Blei,
486 D. M., and Norman, K. A. (2018). A probabilistic approach to discovering dynamic full-brain
487 functional connectivity patterns. *NeuroImage*, 180:243–252.
- 488 [25] Miller, K. J., Shenoy, P., den Nijs, M., Sorensen, L. B., Rao, R. P. N., and Ojemann, J. G. (2008).
489 Beyond the gamma band: the role of high-frequency features in movement classification.
490 *IEEE Transactions on Biomedical Engineering*, 55(5):1634 – 1637.
- 491 [26] Mori, S., Oishi, K., Jiang, H., Jiang, L., Li, X., Akhter, K., Hua, K., Faria, A. V., Mahmood,
492 A., Woods, R., Toga, A. W., Pike, G. B., Neto, P. R., Evans, A., Zhang, J., Huang, H., Miller,
493 M. I., van Zijl, P., and Mazziotta, J. (2008). Stereotaxic white matter atlas based on diffusion
494 tensor imaging in an icbm template. *NeuroImage*, 40(2):570–582.
- 495 [27] Rasmussen, C. E. (2006). *Gaussian processes for machine learning*. MIT Press.
- 496 [28] Sarvas, J. (1987). Basic mathematical and electromagnetic concepts of the biomagnetic
497 inverse problem. *Phys. Med. Biol.*, 32(1):11–22.
- 498 [29] Sawyer, R. J. (1995). *The Terminal Experiment*. HarperPrism.
- 499 [30] Sederberg, P. B., Kahana, M. J., Howard, M. W., Donner, E. J., and Madsen, J. R. (2003). Theta
500 and gamma oscillations during encoding predict subsequent recall. *Journal of Neuroscience*,
501 23(34):10809–10814.
- 502 [31] Sederberg, P. B., Schulze-Bonhage, A., Madsen, J. R., Bromfield, E. B., Litt, B., Brandt,
503 A., and Kahana, M. J. (2007a). Gamma oscillations distinguish true from false memories.
504 *Psychological Science*, 18(11):927–932.

- 505 [32] Sederberg, P. B., Schulze-Bonhage, A., Madsen, J. R., Bromfield, E. B., McCarthy, D. C.,
506 Brandt, A., Tully, M. S., and Kahana, M. J. (2007b). Hippocampal and neocortical gamma
507 oscillations predict memory formation in humans. *Cerebral Cortex*, 17(5):1190–1196.
- 508 [33] Sejnowski, T. J., Churchland, P. S., and Movshon, J. A. (2014). Putting big data to good use
509 in neuroscience. *Nature Neuroscience*, 17:1440–1441.
- 510 [34] Snyder, A. Z. (1991). Dipole source localization in the study of EP generators: a critique.
511 *Electroencephalography and Clinical Neurophysiology*, 80(4):321–325.
- 512 [35] Solomon, E. A., Gross, R., Lega, B., Sperling, M. R., Worrell, G., Sheth, S. A., Zaghloul,
513 K. A., Jobst, B. C., Stein, J. M., Das, S., Gorniak, R., Inman, C., Seger, S., Kragel, J. E., Rizzuto,
514 D. S., and Kahana, M. J. (2018). Mtl functional connectivity predicts stimulation-induced
515 theta power. *Nature Communications*, In press.
- 516 [36] Sporns, O. and Betzel, R. F. (2016). Modular brain networks. *Annual Review of Psychology*,
517 67:613–640.
- 518 [37] Talairach, J. and Tournoux, P. (1988). *Co-planar stereotaxic atlas of the human brain*. Verlag,
519 Stuttgart.
- 520 [38] Tavor, I., Jones, O. P., Mars, R. B., Smith, S. M., Behrens, T. E., and Jbabdi, S. (2016). Task-
521 free MRI predicts individual differences in brain activity during task performance. *Science*,
522 352(6282):216–220.
- 523 [39] Tomasi, D. and Volkow, N. D. (2011). Association between functional connectivity hubs
524 and brain networks. *Cerebral Cortex*, 21:2003–2013.
- 525 [40] Turk-Browne, N. B. (2013). Functional interactions as big data in the human brain. *Science*,
526 342:580–584.

- 527 [41] Weidemann, C. T., Kragel, J. E., Lega, B. C., Worrell, G. A., Sperling, M. R., Sharan, A. D.,
528 Jobst, B. C., Khadjevand, F., Davis, K. A., Wanda, P. A., Kadel, A., Rizzuto, D. S., and Kahana,
529 M. J. (2018). Neural activity reveals interactions between episodic and semantic memory
530 systems during retrieval. *Journal of Experimental Psychology: General*, In press.
- 531 [42] Yeo, B. T. T., Krienen, F. M., Sepulcre, J., Sabuncu, M. R., Lashkari, D., Hollinshead, M.,
532 Roffman, J. L., Smoller, J. W., Zollei, L., Polimieni, J. R., Fischl, B., Liu, H., and Buckner,
533 R. L. (2011). The organization of the human cerebral cortex estimated by intrinsic functional
534 connectivity. *Journal of Neurophysiology*, 106(3):1125–1165.